



Research Paper

A multiphysics model of the electroslag rapid remelting (ESRR) process

E. Karimi-Sibaki^a, A. Kharicha^{a,b}, M. Wu^{a,b,*}, A. Ludwig^b, J. Bohacek^b, H. Holzgruber^c,
B. Ofner^c, A. Scheriau^c, M. Kubin^c

^aChristian-Doppler Laboratory for Advanced Process Simulation of Solidification and Melting, Montanuniversitaet of Leoben, Franz-Josef-Str. 18, A-8700 Leoben, Austria

^bChair of Simulation and Modeling of Metallurgical Processes, Montanuniversitaet of Leoben, Franz-Josef-Str. 18, A-8700 Leoben, Austria

^cINTECO Melting and Casting Technologies GmbH, 8600 Bruck/Mur, Austria

HIGHLIGHTS

- The first 3D model to study multiphysics in an industrial ESRR process.
- The MHD, thermal, and solidification in the ESRR are investigated.
- The impact of formation of the slag skin on the electric current path is analyzed.
- A fairly symmetric melt pool profile of the billet ingot is observed.
- Modeling results are verified by experiments.

ARTICLE INFO

Article history:

Received 18 August 2017

Revised 27 October 2017

Accepted 20 November 2017

Available online 22 November 2017

Keywords:

Electroslag rapid remelting (ESRR)

Electroslag remelting (ESR)

Numerical modeling

Electric current path

Billet ingot

Melt pool profile

Slag skin

ABSTRACT

This paper presents a numerical model (3D) incorporating multiphysics for an electroslag rapid remelting (ESRR) process of industrial scale. The electromagnetic field is calculated in the whole system including the electrode, molten slag, ingot, graphite ring, and mold; the interaction between the turbulent flow and electromagnetic field is calculated for all fluid domains (molten slag and melt pool); the thermal field is calculated in the molten slag, ingot and mold. The solidification of the billet ingot and the formation of solid slag skin layer along the T-mold are considered as well. The formation of the skin layer adjacent to the T-mold can remarkably impact the electric current path in the whole system. The modeling result indicates that no skin layer would form on the graphite ring, as the local electric current density is very high. In contrast, a thick slag skin layer forms along the inclined part of the T-mold, blocks the electric current path there. Those modeling results are verified by experiments. A typical non-axis symmetry flow/thermal field in the slag region, which has been observed in-situ from the slag surface during operation, is predicted. Detailed analyses of the quasi-steady state results of flow/thermal fields are presented. A symmetric melt pool (profile of the solidifying mushy zone) of the ingot is predicted, which agrees with the experiments.

© 2017 Published by Elsevier Ltd.

1. Introduction

The electroslag remelting (ESR) is widely used for further purification of special steels after the primary extraction and refining operations. It is a method of refining a consumable metal electrode through a molten slag as heated electrically [1]. Nowadays, the conventional ESR process can be slightly modified to manufacture ingots with different characteristics. As such, numerous industrial processes were developed. The most well-known among them are

ESR with multiple electrodes [2,3], ESR with electrode change technology [4], current conductive mold (CCM) [5], Pressure-ESR (PESR) [6], ESR for hollow ingot [7,8], and electroslag rapid remelting (ESRR) [9].

A Schematic of ESRR is shown in Fig. 1(a). A T-shape mold, with an embedded graphite ring to collect the electric current, is used. The key concept of ESRR is to combine the high production efficiency of continuous casting technique with the high ingot quality of ESR process. The conventional ESR process has a drawback of low production efficiency.

Based on industrial praxis, the melt rate (in kg/h) of electrode in conventional ESR is strictly chosen as a portion of (0.6–1) ingot diameter (in mm). As such, production of ingots with diameter lower than 400 mm through ESR is very limited (very low melting

* Corresponding author at: Christian-Doppler Laboratory for Advanced Process Simulation of Solidification and Melting, Montanuniversitaet of Leoben, Franz-Josef-Str. 18, A-8700 Leoben, Austria.

E-mail address: menghuai.wu@unileoben.ac.at (M. Wu).

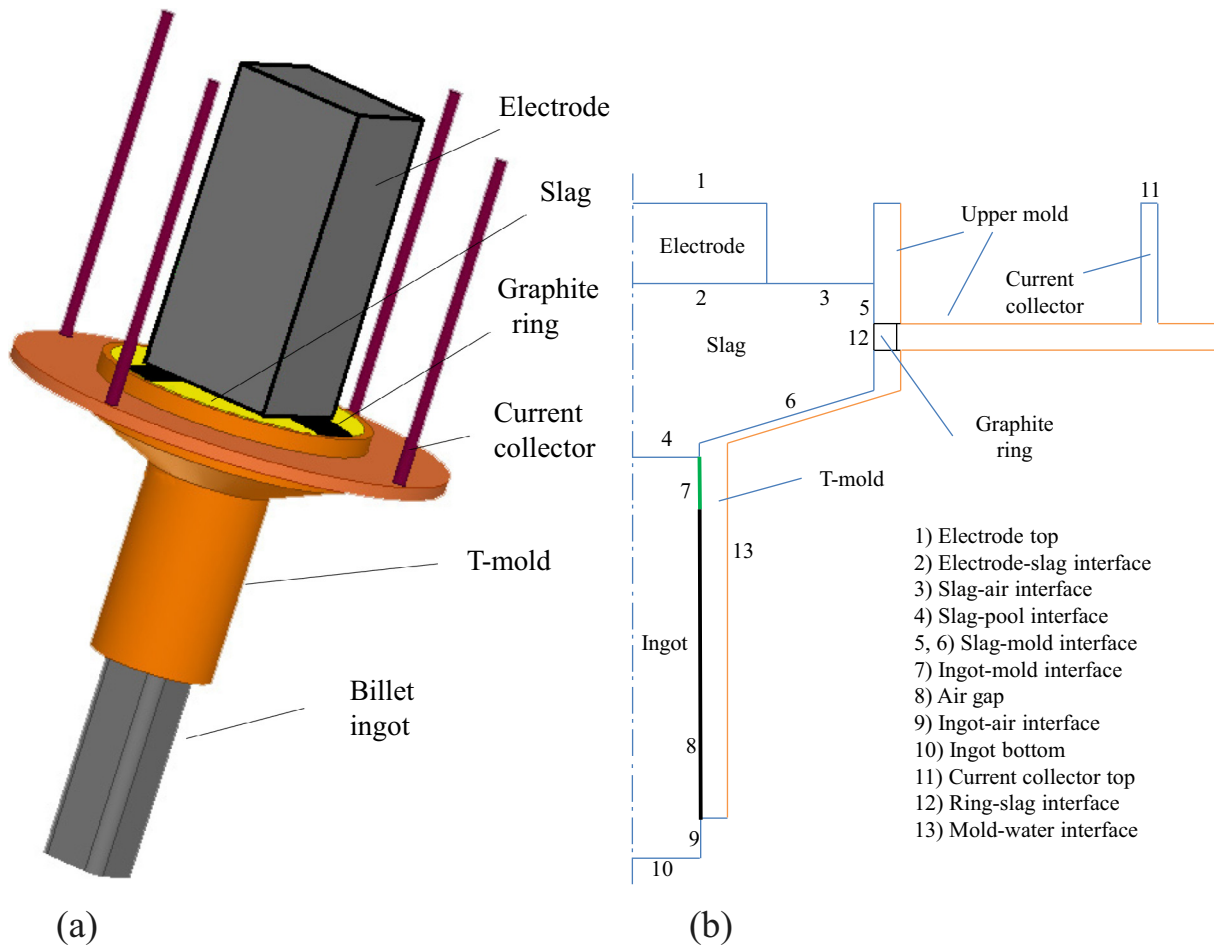


Fig. 1. (a) Schematic of the ESRR process and the configuration of its computational domain. The graphite ring is placed on the mold wall a few centimeters below the slag free surface. The electromagnetic field is calculated in the whole domain including electrode, slag, graphite ring, current collector, T-mold and billet ingot. The thermal/solidification field is calculated in the slag, mold, and ingot. The velocity field is calculated in the slag and ingot. (b) A cross-section of the ESRR process is shown to mark different material regions and corresponding interfaces/boundaries. The calculation is performed in the full 3D.

rate) and uneconomical despite of their wide application area. On the other hand, this ratio for the ESRR can be increased to 3–10, namely ca. 10 times higher [10]. There are only a few monographs available discussing about the ESRR process. A comprehensive description of the process was given by Holzgruber [9]. Alghisi et al. [11] reported the first ESRR process with the continuous casting concept using automatic manipulator at the beginning of this century. Nowadays, the on-going research on the ESRR process focuses on the optimization of the T-shape mold. The overall energy loss through the mold is still high, and it must be reduced [12].

Experimental analysis and measurements are impossible for the ESRR process during operation because of high degree of opacity of materials at the elevated temperature of the process ($\sim 1900^\circ\text{C}$). Actually, simulation is nowadays the only way to get insight into the invisible phenomena. Therefore, the industry can directly benefit from the numerical simulation, e.g. to minimize the failure rate, to improve the technology, and to increase productivity. No numerical model for the ESRR has been reported. Here, we propose a comprehensive model to incorporate the multiphysics such as electromagnetic, thermal/solidification, and flow fields. The electromagnetic field is calculated in the whole system including the electrode, molten slag, ingot, graphite ring, and mold. The interplay between the electromagnetic field with the turbulent flow in the molten slag and melt pool regions is taken into account. The thermal field is calculated in the molten slag, ingot and mold.

Furthermore, the model includes the formation of solidified slag layer near the T-mold as well as the solidification of the billet ingot. Details of the analyses for the flow, electromagnetic, and thermal/solidification fields are presented. Experimental results regarding to the marked melt pool profile are used to validate the model. The main goal is through the numerical modeling to obtain fundamental understanding of the ESRR process, hence to aid engineers to optimize the process design and operation parameters.

2. Modeling

2.1. Governing equations

The ESRR process involves a wide range of physical phenomena such as heat transfer with phase change (solidification/melting), and the interaction between flow and electromagnetic field known as magnetohydrodynamics (MHD). Customarily, the Finite Element Method (FEM) is used to solve the governing equation of the electromagnetic field [13,14]. The fluid flow, heat transfer and solidification are simulated using the well-known Finite Volume Method (FVM). For that purpose, the commercial CFD software, FLUENT ANSYS v.14.5, is employed. Some special modeling equations (e.g. to model solidification) are implemented using User-defined-functions (UDF). Over last decade, numerous models were devel-

oped for the conventional ESR process. The model features as the base for the present investigation were actually verified with experimental results for the standard ESR processes of different sizes [15–19]. From modeling point of view, the major difference between the standard ESR and ESRR processes is the configuration of the mold.

Dealing with governing equations of the flow, heat transfer, and electromagnetism in all details of full 3D domain requires enormous computational resources [15,20,21]. For instance, a 3D calculation of the slag region including effects of slag-pool interface movement, formation, departure, and dripping of droplets (by melting the electrode) through the slag for an industrial ESR ingot (600 mm) took six months on a multi-CPU high performance computer cluster (24 cores) for a duration of only five seconds [20]. As such, for the ESRR model, following assumptions are made to allow the 3D calculation feasible:

- (i) The electromagnetic field is calculated independently from the thermal and flow fields. In other words, one-way coupling is assumed in which only the electromagnetic field impacts thermal/flow field.
- (ii) At the top edge of the billet ingot, where the metal is still in liquid state or the as-solidified shell is still 'soft', an ideal contact with the mold is assumed. After that, the as-solidified shell shrinks away from the mold and the ingot-mold contact gets lost to form an air gap. This air gap is treated by considering an effective heat transfer coefficient [15]. The height of the contact zone (~ 3 cm) is predefined.
- (iii) The moving fluid-fluid interface is not calculated explicitly. The interface between slag and melt pool is assumed to be stationary. The formation and motion of the melt droplets by melting the electrode is not tracked, hence the influence of droplets on the global electromagnetic field is ignored. However, the impact of the droplets on the momentum, energy, and mass transfer is implicitly modeled as source terms in corresponding conservatin equations [22,23].

The amount of mass/momentum/energy sources of droplets in the melt pool are assumed to decrease in a linear manner from the slag-pool interface to end of an impact depth (λ). The value of λ can be estimated using direct numerical simulation of droplet-liquid interface splash phenomena or by the experiment. Here, we assumed that the sizes of droplets are constant (~ 1 cm). Correspondingly, the impact depth is estimated to be ca. 15 cm [23]. Therefore, the volumetric mass source of droplets (M) as a function of the vertical position (z), direction of gravity, in the pool is given by

$$M(z) = \frac{2\dot{m}}{\lambda A_{\text{impact}}} \left(1 - \frac{z}{\lambda}\right) \quad (1)$$

where (\dot{m}) is melt rate of electrode, (z) is the z-coordinate value relative to the slag-pool interface in the melt pool, and (A_{impact}) denotes the area where droplets enter to the pool. The latter is equivalent to the electrode area since the droplets are assumed to enter the pool under the shadow of electrode.

After computing the mass source of droplets (M), one can simply obtain the momentum source in the melt pool (Mu_{impact}) considering that (u_{impact}) is the terminal velocity of droplets (~ 0.35 m·s⁻¹). Similarly, the energy source of droplets in the pool is defined according to: $M\bar{C}_p T_{\text{impact}}$, where (T_{impact}) is the calculated average temperature of slag-pool interface in the impact area, and (\bar{C}_p) is the average heat capacity of metal droplets (~ 820 J·kg⁻¹·K⁻¹).

The momentum/energy source terms to model the impact of droplets in the slag zone under the shadow of electrode are also

considered. Note that, droplets absorb energy/momentum in the slag zone, and they release energy/momentum in the melt pool. Therefore, the amounts of energy/momentum sources of droplets in the slag zone must be equal to those in the melt pool but opposite in the sign in order to satisfy the energy/momentum conservations [22,23].

Illustratively, a cross-section of the ESRR process is shown in Fig. 1(b), marking different material regions and corresponding interfaces/boundaries.

2.1.1. Electromagnetic field

The A - ϕ formulation is employed to calculate the electromagnetic field [13,14], where ϕ is the electric scalar potential and \vec{A} denotes the magnetic vector potential. The method is very robust and accurate to model the current path including mold current and eddy current. The electric scalar potential is obtained by solving the conservation equation of electric current:

$$\nabla \cdot \vec{j} = 0. \quad (2)$$

The current density (\vec{j}) includes two parts:

$$\vec{j} = -\sigma \nabla \phi - \sigma \frac{\partial \vec{A}}{\partial t}. \quad (3)$$

The first right-hand-side (RHS) term of Eq. (3) is the imposed electric current, as calculated from the electric scalar potential by considering the electric conductivity of material (σ). The second RHS term describes the effect of eddy currents.

The magnetic field (\vec{B}) is computed by solving the equation of magnetic vector potential that is expressed as:

$$\vec{B} = \nabla \times \vec{A}, \quad (4)$$

$$\text{while } \vec{j} = \nabla \times \left(\frac{1}{\mu_0} \nabla \times \vec{A} \right) - \nabla \left(\frac{\lambda_p}{\mu_0} \nabla \cdot \vec{A} \right). \quad (5)$$

Here, the Coulomb gauge ($\nabla \cdot \vec{A} = 0$) is used to obtain a unique solution [14]. The displacement currents are ignored and the magnetic permeability (μ_0) is assumed to be constant ($4\pi \times 10^{-7}$ J·m⁻¹·A⁻²).

The second RHS term of Eq. (5) is included as a penalty function term in an ad-hoc manner to enforce the zero divergence of the magnetic field [24–26]. The value for penalty factor (λ_p) must be chosen as small as possible, typically in the range between zero and one, to quickly drive the linear system toward the divergence free solution [26].

Finally, Lorentz force (\vec{F}_L) and the Joule heat (Q) are explicitly computed and added as source terms for the momentum and energy conservation equations respectively.

$$\vec{F}_L = \vec{j} \times \vec{B}, \quad (6)$$

$$Q = \frac{|\vec{j}|^2}{\sigma}. \quad (7)$$

The required boundary conditions for electric scalar potential and magnetic vector potential (axial, radial, and tangential components) are assigned [18]. A condition of free of eddy currents for surrounding region is considered (\sim three times larger than mold diameter), where the magnitude of vector potential is set to zero. Therefore, continuity of electric and magnetic potentials is applied at all interfaces between zones. A value of zero for electric scalar potential as well as magnetic induction flux is applied at ingot

bottom, and top of current collectors. The magnetic induction flux is zero for electrode top, whereas the flux of electric potential is prescribed [26].

2.1.2. Thermal field and solidification

The temperature field is calculated by solving an enthalpy (h) conservation equation:

$$\frac{\partial}{\partial t}(\rho h) + \nabla \cdot (\rho \vec{u} h) = \nabla \cdot (\lambda_{\text{eff}} \nabla T) + Q + S. \quad (8)$$

where ρ denotes the density, \vec{u} the velocity of the liquid-solid mixture, λ_{eff} the effective thermal conductivity including the effect of turbulence, and S is the source term for treating the solidification latent heat. It includes two parts:

$$S = -\frac{\partial}{\partial t}(\rho f L) - \rho \vec{u}_s \cdot \nabla f_1. \quad (9)$$

Hear, u_s is the casting velocity and f_1 denotes the liquid volume fraction. L is the heat of fusion. The steel is treated as an effective binary Fe-C alloy system, and the alloy element C is very diffusive in both liquid and solid. Therefore, lever rule [27] is employed to calculate the liquid volume fraction as a function of temperature,

$$f_1 = \begin{cases} 1 & T > T_{\text{liquidus}} \\ 1 - [(T_{\text{liquidus}} - T) / ((T_f - T)(1 - k_p))] & T_{\text{solidus}} < T \leq T_{\text{liquidus}} \\ 0 & T \leq T_{\text{solidus}} \end{cases} \quad (10)$$

T is temperature, T_f is the melting point of solvent (1811 K), k_p is the partition coefficient (0.35), T_{liquidus} and T_{solidus} are the liquidus and solidus temperatures of the alloy.

The thermal field is calculated in the slag, mold and ingot region, thus appropriate interfacial heat transfer conditions must be assigned between those zones. A comprehensive description of required thermal boundary conditions is given in Ref. [15]. A crust of solidified slag, called slag skin layer, forms a mold lining which separates the molten slag from the T-mold. No slag skin was observed during the operation between the billet and the mold (skin thickness ~ 0) that is taken into account in the model. However, the formation of solid slag layer in the T-mold is implicitly simulated. For that purpose, a balance of thermal resistance and Joule heat as created in the solid skin is performed. A one-dimensional equation for the skin layer thickness (δ) along the T-mold can be extracted [28]:

$$\delta \frac{j^2}{\sigma_{\text{skin}}} + Q_{\text{slag}} - Q_{\text{mold}} = 0, \quad (11)$$

where (σ_{skin}) denotes the slag skin electrical conductivity, (Q_{slag}) the heat flux coming from the liquid slag, and (Q_{mold}) the heat entering to the mold.

2.1.3. Turbulent flow field

The continuity and momentum equations are solved:

$$\frac{\partial \rho}{\partial t} + \nabla \cdot (\rho \vec{u}) = 0, \quad (12)$$

$$\frac{\partial}{\partial t}(\rho \vec{u}) + \nabla \cdot (\rho \vec{u} \vec{u}) = -\nabla p + \nabla \cdot (\mu_{\text{eff}}(\nabla \vec{u} + \nabla \vec{u}^T)) + \rho_0 \times \vec{g} \beta (T - T_0) + \vec{F}_L. \quad (13)$$

where p denotes the pressure, μ_{eff} the effective viscosity, \vec{g} the gravity, β the thermal expansion coefficient, ρ_0 and T_0 are reference density and reference temperature for calculating the buoyancy. Boussinesq approximation is used to model the thermal buoyancy in the slag and melt pool regions.

The turbulence is calculated using the Scale-Adaptive Simulation (SAS) model [29], which is an improved version of the shear stress transport (SST-K- ω) turbulent model [30]. The essential feature of SAS model is an effective and accurate near wall treatment as the model is insensitive to the grid spacing of the near wall cells. It is believed that the accuracy of the results using the SAS model is comparable to that of the LES model with the advantage of lower computational cost [29,30].

Non-slip boundary condition is applied at all boundaries in the slag except for the slag-air interface where a free-slip condition is applied. The flow boundary condition surrounding the ingot is similarly no-slip except for the ingot bottom where the velocity is specified to be the casting speed (u_s).

Special care must be taken to accurately model the interdendritic flow inside the ingot mushy zone. The interdendritic flow is modeled based on Darcy's law [31]. An anisotropic permeability following Heinrich and Poirier [32] is employed.

$$K_{\text{Parallel}} = \begin{cases} 3.75 \times 10^{-4} f_1^2 d_1^2 & 0 < f_1 \leq 0.65 \\ 2.05 \times 10^{-7} \left[\frac{f_1}{1-f_1} \right]^{10.739} d_1^2 & 0.65 \leq f_1 \leq 0.75 \\ 0.074 (\ln(1-f_1))^{-1} - 1.49 \\ + 2(1-f_1) - 0.5(1-f_1)^2 d_1^2 & 0.75 \leq f_1 < 1.0 \end{cases} \quad (14)$$

$$K_{\text{Perpendicular}} = \begin{cases} 1.09 \times 10^{-3} f_1^{3.32} d_1^2 & 0 < f_1 \leq 0.65 \\ 4.04 \times 10^{-6} \left[\frac{f_1}{1-f_1} \right]^{6.7336} d_1^2 & 0.65 \leq f_1 \leq 0.75 \\ \left[-6.49 \times 10^{-2} + 5.43 \times 10^{-2} \left[\frac{f_1}{1-f_1} \right]^{0.25} \right] d_1^2 & 0.75 \leq f_1 < 1.0 \end{cases} \quad (15)$$

where d_1 denotes the primary spacing of the dendrite arm ($\sim 200 \mu\text{m}$), and K_{Parallel} and $K_{\text{Perpendicular}}$ are permeability in parallel and perpendicular directions to the primary dendrites respectively.

Note that, primary dendrites grow in the direction of the temperature gradient. Therefore, the unit vector ($\vec{n}_{\parallel} = \frac{\vec{\nabla} T}{\|\vec{\nabla} T\|}$) determines the parallel direction relative to the primary dendrites. As first step, the velocity of the interdendritic melt relative to primary dendrites must be calculated ($\vec{u}_r = \vec{u} - \vec{u}_s$). As second step, the latter is decomposed to the sum of parallel and perpendicular velocity components ($\vec{u}_r = \vec{u}_{\perp} + \vec{u}_{\parallel}$). Then, the parallel velocity component is calculated using the parallel unit vector ($\vec{u}_{\parallel} = (\vec{u}_r \cdot \vec{n}_{\parallel}) \vec{n}_{\parallel}$). Afterwards, one can easily obtain the perpendicular velocity component ($\vec{u}_{\perp} = \vec{u}_r - \vec{u}_{\parallel}$). In a similar manner to find the parallel direction, the unit vector in perpendicular direction can be obtained: $\vec{n}_{\perp} = \frac{\vec{u}_{\perp}}{\|\vec{u}_{\perp}\|}$. The calculated unit vectors are used to determine the drag resistance force in parallel (F_{\parallel}) and perpendicular (F_{\perp}) components,

$$F_{\parallel} = -\frac{\mu}{K_{\parallel}} (\vec{u}_r \cdot \vec{n}_{\parallel}) \quad (16)$$

$$F_{\perp} = -\frac{\mu}{K_{\perp}} (\vec{u}_r \cdot \vec{n}_{\perp}) \quad (17)$$

Eventually, they are used to calculate the drag resistance force in the mushy zone (F_p) which is added as an extra sink term in Eq. (13) in the ingot domain.

$$\vec{F}_p = (F_{\perp}) \vec{n}_{\perp} + (F_{\parallel}) \vec{n}_{\parallel} \quad (18)$$

2.2. Simulation setup

Following the industrial process, an alternating current (AC) with a frequency of 50 Hz was imposed to the system. A large uncertainty of the electric or thermal properties of the slag exists due to the difficulty of the measurement at the elevated temperature (~ 2000 K) of the process. The electric conductivity of conventional slags in liquid state was reported to vary in the range between 80 and $300 \Omega^{-1}\cdot\text{m}^{-1}$ [33]. The electric conductivity of the solid slag skin layer is unknown. Based on the ESRR industry practices, nearly 90% of the current is collected in the graphite ring and only a small portion of current ($\sim 10\%$) flows through the ingot. Accordingly, the solidified slag skin layer is not a perfectly electrical insulator. A laboratory measurement using impedance spectroscopy suggested that the skin layer during the operation at elevated temperature (~ 800 – 1500 K) conducts electricity with the electric conductivity in the range between 0.01 and $10 \Omega^{-1}\cdot\text{m}^{-1}$. This parameter governs the amount of the mold current [22,34].

The thermal field in the whole process is greatly influenced by thermal conductivity of the slag. Approximate values for thermal conductivity of CaF_2 -based slags at elevated temperatures are reported to be between 0.5 and $5 \text{ W}\cdot\text{m}^{-1}\cdot\text{K}^{-1}$ [35,36]. For our simulations, we considered both reported values in the literature and the industrial measurements of material properties which are temperature dependent. The averaged material properties of the slag and steel as well as operating conditions are listed in Table 1.

A total number of 1.2 million mesh elements are used for full 3D calculation. Transient calculation is made, but only the result of quasi-steady state is evaluated. The calculation needs approximately one month using a multi-CPU cluster (24 cores, parallel computing).

3. Results

The current path in a cross-section is shown in Fig. 2(a). The electric current tends to flow along the surface of the mold as a result of the large electrical conductivity of the copper mold (skin effect). Major electric current ($\sim 90\%$) is taken by the graphite ring, whereas a small portion of the electric current ($\sim 10\%$) crosses the ingot-mold interface and then flows toward the bottom of ingot. Almost no current enters to the mold through the inclined part of the T-mold where a relatively thick skin layer forms (in average ~ 4 mm). In contrast, a very thin layer of skin forms near the

Table 1
Parameters used for the calculations.

Material properties	Slag	Steel
ρ ($\text{kg}\cdot\text{m}^{-3}$)	2440	7000
μ (Pa·s)	0.01	0.0062
c_p ($\text{J}\cdot\text{kg}^{-1}\cdot\text{K}^{-1}$)	1255	820
λ ($\text{W}\cdot\text{m}^{-1}\cdot\text{K}^{-1}$) liquid state	4	35
λ ($\text{W}\cdot\text{m}^{-1}\cdot\text{K}^{-1}$) solid state	0.5	16
β (K^{-1})	0.0001	0.00011
T_{liquidus} (K)	1715	1773
T_{solidus} (K)	1598	1668
σ ($\Omega^{-1}\cdot\text{m}^{-1}$) liquid state	130	8.8×10^5
σ ($\Omega^{-1}\cdot\text{m}^{-1}$) solid state	0.1	8.8×10^5
Operation parameters		
Ingot size (mm)	165×165	
Electrode size (mm)	332×265	
T-mold diameter (mm)	580	
Slag height (mm)	213	
Melt rate ($\text{kg}\cdot\text{h}^{-1}$)	400	
RMS current (kA)	16	
AC frequency (Hz)	50	
Power (MW)	1.0	

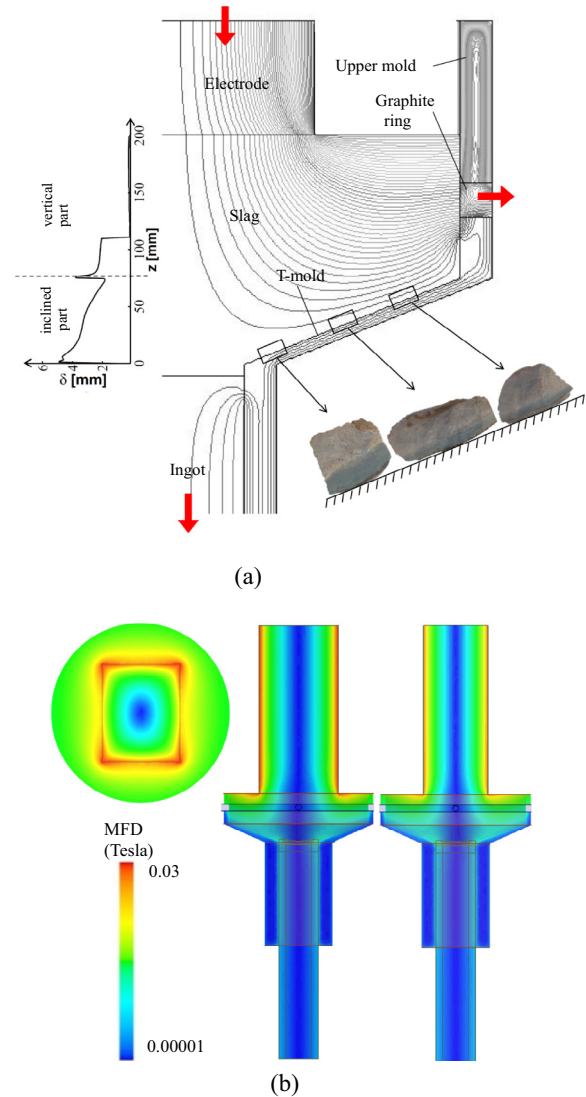


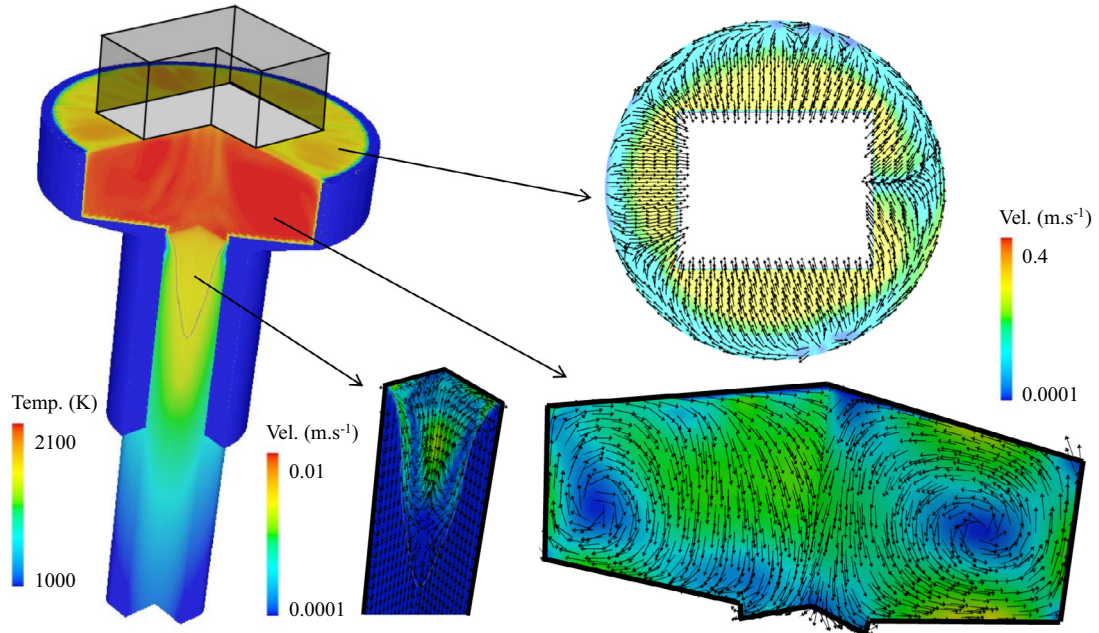
Fig. 2. (a) The electric current path is shown in a cross-sectional cut. Red arrows indicate the input/output direction of electric current. Additionally, the calculated skin thickness along the z-coordinate of the T-mold is inserted. Samples of the as-solidified slag were collected and shown for three different locations along the inclined part of the T-mold. The dark grey layer indicates the slag skin layer; (b) The time-averaged magnetic flux density (MFD) is shown at different cross-sections: top-view (slag surface and electrode), front-view (big section of electrode, slag, T-mold, and ingot), and side-view (small section of electrode, slag, T-mold, and ingot). (For interpretation of the references to color in this figure legend, the reader is referred to the web version of this article.)

graphite ring where the current density is very high. The calculated thickness of the skin layer (Eq. (11)) as insert diagram in Fig. 2(a) is also shown. The predicted thickness of the skin layer is validated against the industrial observations. As predicted by the model, no slag skin exists on the graphite ring in the practical operation. In addition, several samples of slag skin were collected from different locations near the inclined part of the T-mold. Photos of the samples of slag skin (dark grey region) are inserted in Fig. 2(a) which confirm/indicate the formation of a thick skin layer (in average ~ 4 mm) along the inclined part of the T-mold. The thickness of the slag skin layer increases from the top (below the graphite ring) toward the bottom (near the ingot) of the T-mold. Fig. 2(b) illustrates the time-averaged electromagnetic field in the whole system. The electromagnetic field is very strong near the edges of the electrode. The magnetic field is found to be stronger near the small side of the electrode in comparison to that near the large side

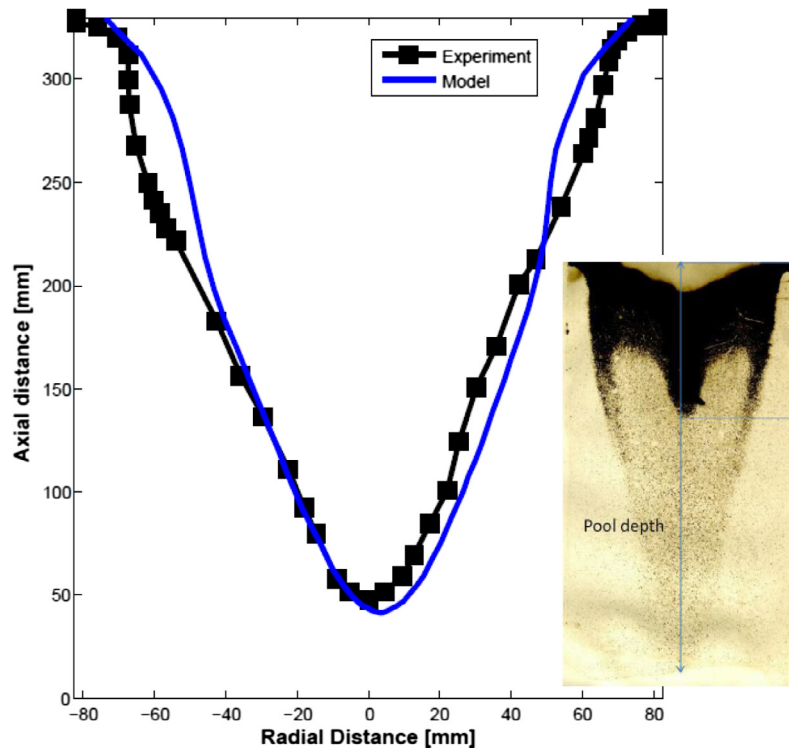
of electrode as a result of the electric skin effect. Additionally, the strength of magnetic field is notable near the inclined part of T-mold where significant electric current flows tangential to the inclined part of the mold. As previously mentioned, the electric

current cannot cross the inclined part of the mold due to formation of a relatively thick skin layer.

The thermal/solidification and flow fields are illustrated in Fig. 3 (a). The flow is rotating (converging flow) under the shadow of



(a)



(b)

Fig. 3. (a) The thermal field in slag, mold, and ingot and iso-line of liquid fraction ($f_l = 0.9$) in the ingot is shown. The magnitude (color scale) and direction of the velocity field in cross-sections of the melt pool, slag, and slag free surface are also illustrated. (b) A comparison is made between the calculated pool profile using the model ($f_l = 0.9$), and the experimental result (Baumann print). The Baumann print of the pool profile is also inserted (Courtesy of Xingtai Iron & Steel Corp. LTD).

electrode in the slag zone where the Lorentz force is dominant. Furthermore, the slag is flowing toward the electrode at slag free surface. Only, a small portion of electric current ($\sim 10\%$) enters the ingot zone. Consequently, the Lorentz force is significantly weaker than the thermal buoyancy and droplets impact in the melt pool. The hot molten metal is continuously flows toward the interface in the bulk of melt pool. However, the molten metal is pushed downward near the wall of the cold mold under the influence of strong buoyancy force.

The flow is strongly turbulent in the slag, especially under the electrode, where a rotational flow exists. As a consequence, the effective thermal conductivity in the slag bulk is significantly increased ($\sim 160 \text{ W}\cdot\text{m}^{-1}\cdot\text{K}^{-1}$). Similarly, a turbulent flow exists in the melt pool where the effective thermal conductivity is predicted to be around $75 \text{ W}\cdot\text{m}^{-1}\cdot\text{K}^{-1}$. Therefore, both turbulence enhanced effective conductivities and mean flow advection contribute to the thermal field. Principally, the heat transfer is very efficient in the melt due to rigorous mixing of the flow. Therefore, a relatively uniform temperature field in the bulk of slag and melt pool is observed.

The internal quality of the ingot is highly dependent on the shape and depth of melt pool. The desired outcome is a shallow melt pool that promotes unidirectional (upwards) solidification of the ingot and formation of segregation-minimal alloy. Therefore, the melt pool profile is most often used indicator for the internal quality of the ingot [38,39]. The predicted pool profile by the model is compared with the experiment, as shown in Fig. 3(b). In the experiment, a postmortem analysis of the as-cast structure with the method of Baumann print was made to mark the melt pool profile. A good agreement is observed in the shape of the melt pool between the simulation and experimental results. The major discrepancy between simulation and experimental results is found near the mold wall in the vicinity of slag-pool interface where the progress of solidification front is overestimated by the model. Note that, the movement of slag-pool interface is not included in the model. The moving interface certainly intensifies the flow in the melt that in turn enhances the global energy transfer in the liquid melt pool. As a consequence, the evolution of the mushy zone might be slowed down in the upper region of the billet.

4. Discussions

Numerous operational parameters can remarkably impact both internal and surface quality of the final ingot. Those parameters are the power supply, the melt rate and immersion depth of the electrode, the type and volume of slag, the current ratio (ratio of graphite ring current to ingot current), and the fill ratio (ratio of electrode to ingot diameter). Some of those parameters are independent, while some others are correlated. The selections of operational parameters are typically made empirically. These trial and error approaches are prohibitively expensive. By using the numerical model, as proposed in this work, the costly trials can be significantly minimized.

The industry targets to optimize the ESRR process by the aid of the numerical model. The main goals are to achieve the highest melt rate (highest production rate), a target pool depth, and a high energy-efficient process. Both conventional ESR and ESRR are not energy-efficient processes [40–42]. Generally, a small portion of the input energy ($\sim 20\%$) is received by the electrode to achieve the target melt rate. Significant portion of the input energy ($\sim 50\%$) is lost at the slag-mold and ingot-mold interfaces through the water-cooled mold. In addition, a notable radiation heat loss ($\sim 20\%$) exists at the slag free surface. Eventually, a small fraction of the total input energy ($\sim 10\%$) reaches to the bottom of the ingot. For this purpose, the optimization must also be related to the

design of mold. It is believed that the angle of the inclined part of T-mold can affect the overall energy loss through the mold. The thickness and location (distance to slag free surface) of the graphite ring must be carefully opted to prolong its life and to avoid mold damage. Additionally, the electric current must be homogeneously collected through the graphite ring, as it is favorable to the ingot surface/internal quality. Therefore, further modeling efforts are still demanded.

We should also be aware of the fact that some other factors influence the quantitative accuracy of the modeling results. For instance, significant uncertainties exist related to physicochemical properties of both the slag and alloy [37]. It is difficult to measure those properties at elevated temperature, and they are strongly dependent on temperature and composition [43]. As previously mentioned in “III. Results”, assuming a stationary slag-pool interface influences the modeling results. Nevertheless, this assumption is essential to reduce significantly the computational cost. For the sake of simplicity, the height of the contact zone between ingot and mold was predefined. This assumption may influence the predicted slope of the pool profile especially near the mold wall. Modeling the shrinkage of the material and subsequent formation of the air gap is quite a challenging problem [44,45]. Combined mechanical and thermal forces which are acting on the solid ingot must be evaluated.

Due to the high computational cost (one month of parallel computing with 24 cores for each simulation run), no systematical parameter study is performed in this paper. Although the calculated solidification pool profile of the ingot agrees with the experimental one, we believe that details of the turbulent flow, especially in the slag region, are still sensitive to the grid resolution. It is not possible to obtain a grid convergent result regarding to the flow field based on the current computation resources. Additionally, although many other parameters such as materials properties, boundary conditions, and different option of turbulence models were determined/chosen with our best knowledge, further parameter studies on the sensitivity of the modeling results to those parameters are desirable.

In spite of the model simplifications and assumptions, which are necessary at the current stage, the proposed model provides valuable information about the transport phenomena and solidification in the ESRR. The insight of the process with multiphysics nature can be analyzed quantitatively.

5. Summary

Electroslag rapid remelting (ESRR) is a secondary metallurgical process which is used to manufacture billet ingots at high production rate in a cost-effective way. The system includes a graphite ring which is placed on the wall of a T-mold. The graphite ring is served to collect the major amount ($\sim 90\%$) of the electric current that flows through the whole system. Reports on this topic are scarce. Thus, a model is demanded to get insight into the process. For this purpose, a multiphysics model considering the computational efficiency is proposed to investigate the transport phenomena in the ESRR. Calculation of the electromagnetic field including the electrode, molten slag, graphite ring, ingot and mold is carried out. The model takes into account the interaction between the turbulent flow and electromagnetic field in the fluid region. The thermal field in the molten slag, ingot and mold is computed. Additionally, the solidification of the billet ingot as well as the formation of solid slag skin layer along the T-mold is included.

Detailed analyses of formation of the slag skin layer and subsequently the electric current path in the whole system are presented. No skin layer forms on the graphite ring where the current density is very high. In contrast, a thick skin layer is pre-

dicted along the inclined part of the T-mold where a tiny amount of current can cross the skin layer. The modeling result is evidenced by the corresponding industry observations. The global heat transfer is very efficient in the melt. As a consequence, the pool profile of the ingot tends to become stable and symmetric. Results on the melt pool profile are validated against the experiment.

Acknowledgements

The authors acknowledge the financial support by INTECO melting and casting technologies GmbH and Austrian Federal Ministry of Economy, Family and Youth and the National Foundation for Research, Technology and Development within the framework of the Christian Doppler Laboratory for Advanced Process Simulation of Solidification and Melting.

References

- [1] G. Hoyle, *Electroslag Processes*, Applied Science Publishers, London, UK, 1983.
- [2] Y. Dong, Z. Jiang, H. Liu, R. Chen, Z. Song, *ISIJ Int.* 52 (12) (2014) 2226.
- [3] B. Li, B. Wang, F. Tsukihashi, *Metall. Mater. Trans. B* 45 (2014) 1122.
- [4] E. Karimi-Sibaki, A. Kharicha, M. Wu, A. Ludwig, H. Holzgruber, B. Ofner, A. Scheriau, M. Kubin, M. Ramprecht, *Mater. Sci. Eng.* 143 (2016) 012006, <https://doi.org/10.1088/1757-899X/143/1/012006>.
- [5] H. Holzgruber, W. Holzgruber, A. Scheriau, M. Knabl, M. Kubin, J. Korp, R. Pierer, In: *Liquid Metal Processing and Casting (LMPC)*, 2011, Nancy, p. 57.
- [6] A.D. Patel, J. Reitz, J. H. Magee, R. Smith, G. Maurer, B. Friedrich, In: *Liquid Metal Processing And Casting (LMPC)*, 2009, Santa Fe, p. 253.
- [7] L. Medovar, G. Stovpchenko, G. Dudka, A. Kozminskiy, B. Fedorovskii, V. Lebid, I. Gusiev, in: *Liquid Metal Processing And Casting (LMPC)*, 2013, Austin, p. 137.
- [8] X. Chen, F. Liu, Z. Jiang, H. Li, X. Zang, X. Deng, *J. Iron Steel Res.* 22 (3) (2015) 192.
- [9] H. Holzgruber, PhD Thesis, Montanuniversitaet, Leoben, Austria, 2005.
- [10] M. Kubin, A. Scheriau, M. Knabl, H. Holzgruber, in: *AISTech*, 2014, Indianapolis.
- [11] D. Alghisi, M. Milano, L. Paziienza, in: *Metall. Proc. Tech.*, 2005, Riva del Garda.
- [12] C. Deville-Cavellin, A. Scheriau, in: *Liquid Metal Processing And Casting (LMPC)*, 2015, Leoben, p. 79.
- [13] K. Preis, I. Bardi, O. Biro, C. Magele, W. Renhart, K.R. Richter, G. Vrisk, *IEEE Trans. Magn.* 27 (1991) 3798.
- [14] H. Song, N. Ida, *IEEE Trans. Magn.* 27 (1991) 4012.
- [15] E. Karimi-Sibaki, A. Kharicha, J. Bohacek, M. Wu, A. Ludwig, *Adv. Eng. Mater.* 18 (2016) 224.
- [16] A. Kharicha, M. Wu, A. Ludwig, M. Ramprecht, H. Holzgruber, *CFD Modeling and Simulation in Materials*, Wiley Interscience, 2012, p. 139.
- [17] E. Karimi-Sibaki, A. Kharicha, J. Bohacek, M. Wu, A. Ludwig, *Metall. Mater. Trans. B* 46 (2015) 2049.
- [18] A. Kharicha, M. Wu, A. Ludwig, E. Karimi-Sibaki, *Metall. Mater. Trans. B* 47 (2016) 1427.
- [19] E. Karimi-Sibaki, A. Kharicha, J. Korp, M. Wu, A. Ludwig, *Mater. Sci. Forum* 790–791 (2014) 396.
- [20] A. Kharicha, A. Ludwig, M. Wu, 3D simulation of the melting during an electroslag remelting process, in: *EPD Congress*, 2011, San Diego, p. 771.
- [21] Q. Wang, R. Zhao, M. Fafard, B. Li, *Appl. Therm. Eng.* 80 (2015) 178.
- [22] E. Karimi-Sibaki, A. Kharicha, M. Wu, A. Ludwig, H. Holzgruber, B. Ofner, M. Ramprecht, in: *Liquid Metal Processing And Casting (LMPC)*, 2013, Austin, p. 13, https://doi.org/10.1007/978-3-319-48102-9_2.
- [23] A. Kharicha, W. Schützenhöfer, A. Ludwig, R. Tanzer, Selected numerical investigations on ESR process, in: *Liquid Metal Processing And Casting (LMPC)*, 2007, Nancy, p. 113.
- [24] O. Biro, K. Preis, *IEEE Trans. Magn.* 25 (1989) 3145.
- [25] H.Y. Lin, L.M. Tu, L. Udpa, Y.S. Sun, *IEEE Trans. Magn.* 35 (1999) 1354.
- [26] A. Kharicha, M. Wu, A. Ludwig, *ISIJ Int.* 54 (2014) 1621.
- [27] T.W. Clyne, W. Kurz, *Metall. Mater. Trans. A* 12 (1981) 965.
- [28] A. Kharicha, E. Karimi-Sibaki, M. Wu, A. Ludwig, in: *Liquid Metal Processing And Casting Conference (LMPC)*, 2013, Austin, p. 95, https://doi.org/10.1007/978-3-319-48102-9_13.
- [29] F.R. Menter, Y. Egorov, in: *AIAA Paper 2005-1095*, 2005, Nevada.
- [30] F.R. Menter, M. Kuntz, R. Langtry, *Turb. Heat Mass Transf.* 4 (2003) 625.
- [31] M.C. Schneider, C. Beckermann, *Int. J. Heat Mass Transf.* 38 (18) (1995) 3455.
- [32] J.C. Heinrich, D.R. Poirier, *Comptes Rendus Mecanique* 332 (5–6) (2004) 429.
- [33] M. Hajduk, T.E. Gammal, *Stahl und Eisen* 99 (1979) 113.
- [34] M. Hugo, B. Dussoubs, A. Jardy, J. Escaffre, H. Poisson, *Metall. Mater. Trans. B* 47 (2016) 2607.
- [35] R. Taylor, K.C. Mills, *Arch. Eisenhüttenwes* 53 (1982) 55.
- [36] A. Plotkowski, J. deBarbadillo, M.J.M. Krane, *Mater. Sci. Technol.* 32 (12) (2016) 1249.
- [37] A. Kharicha, E. Karimi-Sibaki, M. Wu, A. Ludwig, J. Bohacek, *Steel Res. Int.* (2017), <https://doi.org/10.1002/srin.201700100>.
- [38] E.J. Pickering, *ISIJ Int.* 53 (2013) 935.
- [39] K.O. Yu, J.A. Domingue, G.E. Maurer, H.D. Flanders, *JOM* 38 (1986) 46.
- [40] A. Mitchell, S. Joshi, *Metall. Trans.* 4 (1973) 631.
- [41] M. Choudhary, J. Szekely, *Ironmak. Steelmak.* 8 (5) (1981) 225.
- [42] W. Holzgruber, *Symp. on Special Melting Technologies*, Düsseldorf, 1999, p. 14.
- [43] M. Allibert, H. Gaye, J. Geiseler, D. Janke, B. J. Keene, D. Kirner, M. Kowalski, J. Lehmann, K. C. Mills, D. Neuschütz, R. Parra, C. Saint-Jours, P. J. Spencer, M. Susa, M. Tmar, E. Woermann, *Slag Atlas*, Verlag Stahleisen GmbH, 1995, Düsseldorf, Germany.
- [44] D. Baroudi, A. Ferrantelli, K. YuanLi, S. Hostikka, *Combust. Flame* 182 (2017) 206.
- [45] N. Giesselmann, A. Rückert, M. Eickhoff, H. Pfeifer, J. Tewes, J. Klöwer, *ISIJ Int.* 55 (7) (2015) 1408.